Relationship between hypocentral distributions and Vp/Vs ratio structures inferred from dense seismic array data: a case study of the 1984 western Nagano Prefecture earthquake, central Japan

AUTHOR(S):

Doi, I.; Noda, S.; Iio, Y.; Horiuchi, S.; Sekiguchi, S.

CITATION:

Doi, I. ...[et al]. Relationship between hypocentral distributions and Vp/Vs ratio structures inferred from dense seismic array data: a case study of the 1984 western Nagano Prefecture earthquake, central Japan. Geophysical Journal International 2013, 195(2): 1323-1336

ISSUE DATE:

2013-10-08

URL:

http://hdl.handle.net/2433/179457

Geophysical Journal International

Geophys. J. Int. (2013) **195,** 1323–1336
Advance Access publication 2013 August 30

doi: 10.1093/gji/ggt312

Relationship between hypocentral distributions and *Vp*/*Vs* ratio structures inferred from dense seismic array data: a case study of the 1984 western Nagano Prefecture earthquake, central Japan

Issei Doi,[1] Shunta Noda,[2] Yoshihisa Iio,[1] Shigeki Horiuchi[3] and Shoji Sekiguchi[4]

[1]*Disaster Prevention Research Institute, Kyoto University, Gokasho, Uji, Kyoto* 611-0011, *Japan. E-mail: doi.issei.5e@kyoto-u.ac.jp*
[2]*Railway Technical Research Institute,* 2-8-38 *Hikari-cho, Kokubunji-shi, Tokyo* 185-8540, *Japan*
[3]*Home Seismometer Corporation,* 67-1 *Kamisakai, Tsukuba, Ibaraki* 305-0011, *Japan*
[4]*National Research Institute for Earth Science and Disaster Prevention,* 3-1, *Tennodai, Tsukuba, Ibaraki* 305-0006, *Japan*

Accepted 2013 August 1. Received 2013 July 29; in original form 2013 February 26

SUMMARY

We conducted a three-dimensional traveltime tomographic reconstruction in and around the source region of the 1984 western Nagano Prefecture earthquake to investigate the generation process for the main shock and associated swarm activity. Up to 220 000 high-resolution traveltime records (2 ms error) were compiled from a dense seismic network. From these records, we performed accurate, high-resolution calculations to estimate hypocentre distributions and three-dimensional velocity structure. Most hypocentres aligned along the same path or within the same plane, rather than in three-dimensional clusters. Hypocentres in the swarm region are located in regions with low *Vp*/*Vs* ratios, while few earthquakes occurred in regions with high or normal *Vp*/*Vs* ratios. We suggest that differences in the number of small fractures and fluid content between these two regions influenced the seismic activity. Rupture propagation associated with the main shock appears to be confined by relatively higher *Vp*/*Vs* surroundings, and a low-velocity region which limits its vertical extent.

Key words: Seismic tomography; Fractures and faults; Crustal structure.

1 INTRODUCTION

Elucidating generation processes of earthquakes is critical for long-term forecasting and preparedness. At present, however, we do not fully understand how earthquakes—especially crustal earthquakes, are generated. Recently, studies have posited that the generation mechanism of crustal earthquakes relates to fluids in the crust. Iio *et al.* (2002) suggested that water issuing upwards from subducting slabs drives crustal earthquakes. Vidale & Shearer (2006) and Yukutake *et al.* (2011) also found that fluid diffusion may cause swarm migration.

In studies of heterogeneous structures within the source regions of large earthquakes, low-velocity regions have been found adjacent to the hypocentre. Studies of waves trapped within fault zones found that fractures serve to lower wave velocity in the vicinity of the fault zone (Li *et al.* 1994; Mizuno *et al.* 2004). Using extremely high-density aftershock observations, Okada *et al.* (2006) determined that parts of the 2004 Chuetsu earthquake faults were located in low-velocity regions. Hasegawa *et al.* (2009) reported that low-velocity regions have been detected just beneath the main shock faults of many crustal earthquakes. Moreover, Tian *et al.* (2007) suggest that the existence of fluids weakens the rocks around the faults of crustal earthquakes to trigger large events in California. These studies suggest that fluids beneath the main shock hypocentre migrate into the fault zone and increase the pore pressure to generate the main shock. How fluids interact with subsurface structures, and how these interactions relate to earthquake generation, however, are not fully understood.

In order to investigate the earthquake generation processes, Iio *et al.* (1999) installed a high-density seismic network in and around the source region of the 1984 Nagano Prefecture earthquake. Data from this network enable us to more precisely estimate hypocentre locations and velocity structures. These parameters can, in turn, reveal the behaviour of crustal fluids. In this study, we estimate subsurface three-dimensional velocity structure at ∼1.5 km resolution and interpret relationships among hypocentre distributions and low-velocity anomalies to elucidate generation processes for earthquakes.

2 GEOPHYSICAL SETTING OF THE 1984 WESTERN NAGANO PREFECTURE EARTHQUAKE

The 1984 western Nagano Prefecture earthquake had a Japan Metrological Agency (JMA) magnitude (M_j) of 6.8 and occurred on September 14 about 10 km southeast of Mt. Ontake, an active volcano in central Japan (Fig. 1). The earthquake caused extensive

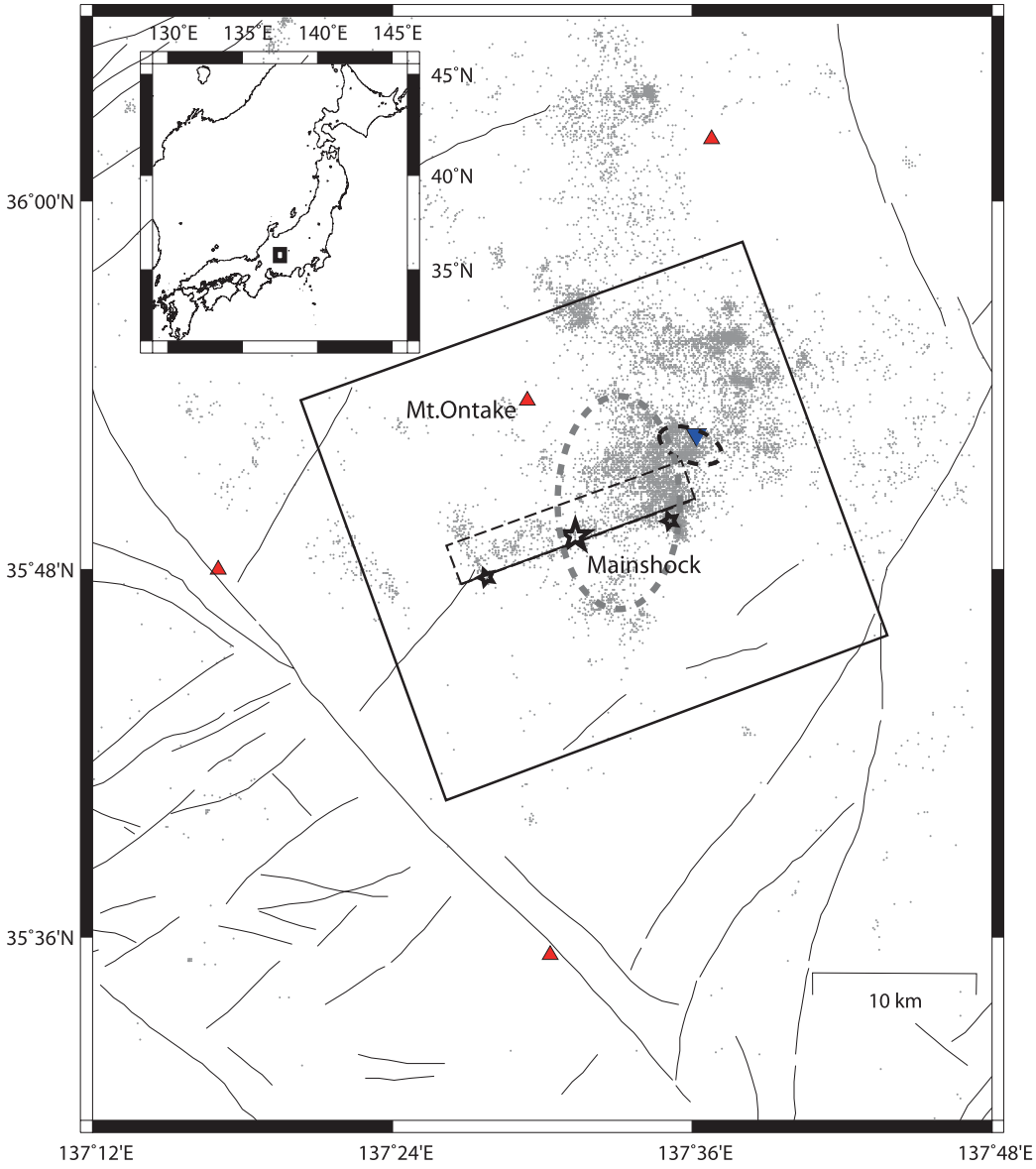

Figure 1. Map showing the area analysed in this study. A large open star and a dashed rectangle mark the main shock epicentre and fault plane (respectively) of the 1984 western Nagano Prefecture earthquake, as estimated by Yoshida & Koketsu (1990). The open rectangle shows the analysis area of this study. Red triangles and solid lines denote Quaternary volcanoes and active faults (Research Group for Active Faults of Japan 1991), respectively. Gray dots indicate epicentres of earthquakes which occurred from 1997 to 2005 at depths of less than 10 km, as entered in the JMA catalog. A gray dashed ellipse denotes the swarm source region before the main shock. Two black small stars represent large aftershocks. A dashed ellipse shows the uplift region estimated by Kimata *et al.* (2004). The blue inverted triangle shows a hydrothermal feature with elevated $\delta^{13}C$ values for CO_2 (Takahata *et al.* 2003).

damage and induced landslides. The earthquake's fault was interpreted by Yoshida & Koketsu (1990) as a right lateral, ENE-WSW trending one.

Ooida *et al.* (1989) investigated the seismicity around the hypocentral region before the main shock occurrence. High seismic activity in the hypocentral region of this earthquake started in May 1978, 1 yr before the eruption of Mt. Ontake. They pointed out that the hypocentral region experienced swarm-type seismicity until this main shock. This swarm activity (denoted by gray-dashed ellipse in Fig .1) first started south of the main shock hypocentre and extended north of it. After the main shock, aftershocks with strike-slip focal mechanisms occurred along the main shock fault. Aftershock activity on the main shock fault was low but M 6.2 and M 5.3 events occurred 10 km western and eastern side of the fault within 20 d, respectively (shown by small stars in Fig. 1). Swarm activity also continued mainly in the northeastern region of the main shock fault and elevated seismic activity continues to the present time with events larger than $M_j \sim 4.0$ occurring about every 2 yr. Fig. 1 shows epicentral distributions from 1997 to 2005 for events shallower than 10 km as listed in the JMA catalog. Seismic activity occurs not only along the main shock fault plane, but also as swarm-like activity in the eastern parts of the source region (Fig. 1). Most of the hypocentres are concentrated in the shallow subsurface at depths of 2–6 km.

Many studies have investigated the structures and mechanisms related to volcanic activity and earthquake generation in this region. Tanaka & Ito (2002) estimated a relatively high crustal heat flow of 70–220 mW m^{-2} for the region and suggested that it confines the depth of hypocentres to the shallow subsurface. Kasaya & Oshiman (2004) and Yoshimura *et al.* (2011) modelled a low-resistivity

region near the main shock hypocentre and swarm region. Takahata *et al.* (2003) detected an anomalous temporal increase during 1996–2000 in $\delta^{13}C$ values of CO_2 from a hydrothermal feature located directly above the swarm, as indicated by the blue inverted triangle in Fig. 1. This study concluded that the enriched fluids originated from the mantle. From levelling observations, Kimata *et al.* (2004) found that 3–6 mm of uplift occurred in the region above the swarm (indicated by a dashed ellipse in Fig. 1) from 2002 to 2004. These workers interpreted the observations according to models showing fluid plumes rising from depths of 1–2 km. These studies also suggest that fluids from the mantle are rising to a depth of about 2 km in and around the main shock source region.

In this region, Hirahara *et al.* (1992) employed approximately 7000 traveltimes from the 1986 Joint University aftershock observation data set and conducted the traveltime tomography to estimate velocity structure with the spatial resolution of 2 km. They found that the low-velocity regions were located in the large amount of dislocation and the retarded rupture front of the main shock fault.

3 DENSE ARRAY DATA

High-density seismic observation has been conducted from 1995 to the present in and around the source region of the 1984 western Nagano Prefecture earthquake (Iio *et al.* 1999). This observation network consists of 57 stations, shown by green squares in Fig. 2. The stations were installed on bedrock in a mountainous region to minimize background seismic noise. The network includes stations spaced at 1–4 km and covers the source region of the main shock and its surrounding swarm activity. Seismic waveforms are recorded at a 10 kHz sampling rate with 16-bit resolution on high- and low-gain channels. The clocks are corrected by GPS every 2 hr such that uncertainties in the absolute time are less than 1 ms. The network's data have allowed highly detailed analyses (e.g. Venkataraman *et al.* 2006; Cheng *et al.* 2007; Yukutake *et al.* 2010) to understand earthquake generation features.

Fig. 3 shows a sample waveform and spectrum recorded by this network. High-frequency (200 Hz) components were contained at high S/N ratio, which provided accurate estimates of *P*- and *S*-wave arrival times. All *P*- and *S*-wave arrival times used in this study were visually estimated. Transverse components were used to visually estimate *S*-wave arrival times so as to reduce the effect of converted waves such as Sp phases.

As shown in Fig. 4, *P*- and *S*-wave arrival times could be estimated to within a few milliseconds to tens of milliseconds, respectively. To examine this more objectively, we compared the visually estimated *P*-wave arrival times with those estimated by a correlation method (e.g. Shearer *et al.* 2005) at station OT01 (open square in Fig. 2). The correlation method uses a template waveform segment starting 0.3 s before and 0.05 s after the *P*-wave arrival time for a reference event with a high S/N ratio. We specifically estimated *P*-wave arrival times from the time when the cross-correlation coefficients with the template waveform attain their maximum for all waveforms recorded at OT01. The difference between the visually estimated *P*-wave arrival times fell within 2 ms of those estimated by the correlation method for ∼90 per cent of traces (Fig. 4c). The consistency of the two estimates indicates that the visually estimated *P*-wave arrival times adhere to rigorous standards of reproducibility.

Stable tomographic inversions require well-constrained hypocentres. We therefore did not use hypocentres with azimuthal gaps greater than 180°. We also ignored hypocentres that had less than 10 traveltimes for either *P*- or *S*-waves. A total of 12 291 events with the magnitude 0.0–3.1 occurring from October 1995 to February 2005 were used along with 215 096 and 183 917 *P*- and *S*-wave traveltimes (respectively). Hypocentres are indicated by solid circles

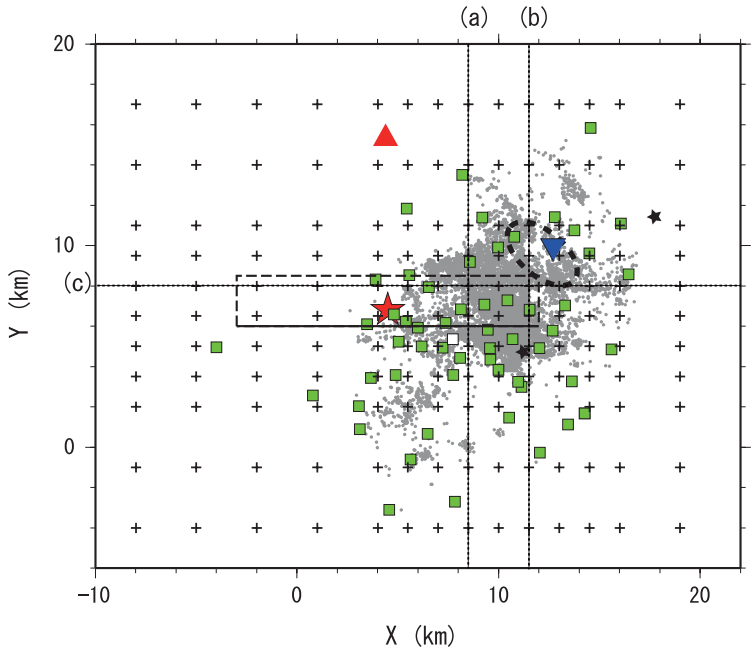

Figure 2. Hypocentre (dots) and station (green squares) distributions used in this study. The origin is located at 137.5°E and 35.75°N. Two black stars represent the locations of quarry blasts used in the refraction analysis (see Section 3). The dotted lines show the cross-sections of the velocity structure shown in Fig. 9. A red star and black rectangles denote the main shock epicentre and the fault plane (respectively) of the 1984 western Nagano Prefecture earthquake as estimated by Yoshida & Koketsu (1990). The dashed ellipse shows the ascending region estimated by Kimata *et al.* (2004) and the blue inverted triangle marks a hydrothermal feature with elevated $\delta^{13}C$ values for CO_2 (Takahata *et al.* 2003).

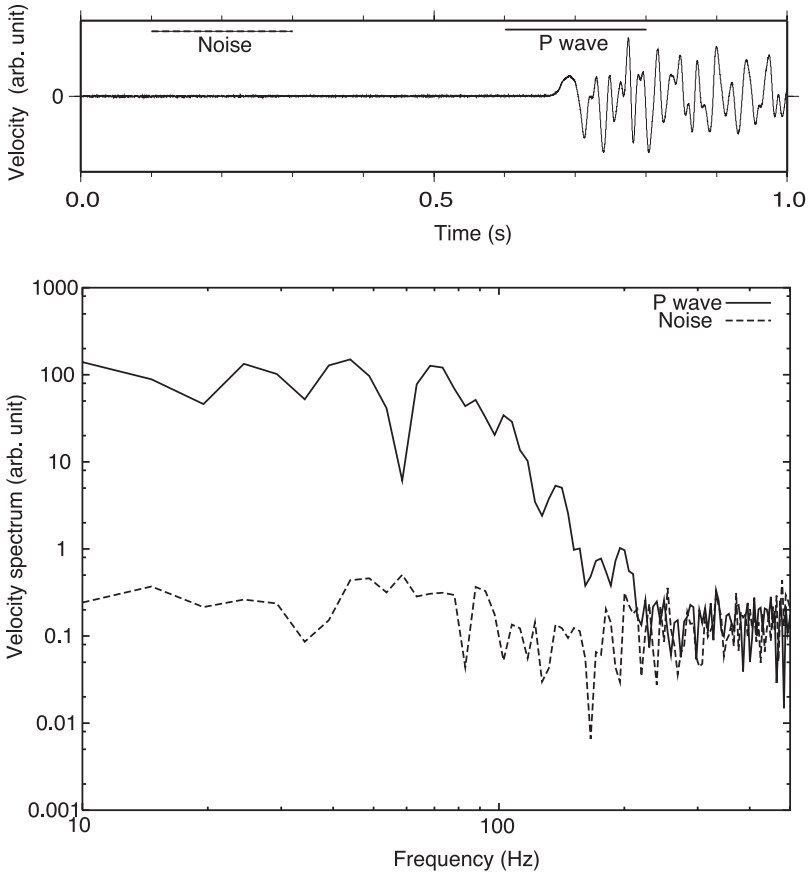

Figure 3. An example of a waveform and spectra observed from the network used in this study (Iio *et al.* 1999). The magnitude of the event was 0.7. Time windows for the pre-signal and *P*-wave arrival shown in the upper panel were used to estimate spectra in the lower panel.

in Fig. 2. The hypocentre locations and velocity structures would be available at greater precision than that used in previous studies (e.g. Hirahara *et al.* 1992) due to the large amount of high-quality data for traveltime tomography in this region. Our data set also has a lot of events in the swarm region, which expects us to obtain detailed velocity structures around there.

4 METHODS

We set the X, Y and Z axes as the strike direction of the main shock fault (N70°E; as estimated in Yoshida & Koketsu 1990), the perpendicular direction and the depth directions, respectively (Fig. 2). The area analysed spanned 32, 26 and 12 km in the X, Y and Z directions, respectively, and included the source region of the main shock and the swarm activity. Figs 2 and 5 show the lateral and vertical grid locations (respectively) used for the three-dimensional inversion. Given errors in the estimated arrival times, horizontal grids were overlaid at 1.5 km intervals in the central part of the analysis area, where many of the hypocentres used in the analysis were located. The grid spacing was 3 km in surrounding areas. Vertical grids were overlaid at 1 km intervals for depths of less than 4 km, and at 2 km intervals for depths greater than 4 km. We set grid's height to 3 km in order to take the station height into account, given that the regolith extends to about this height. The slowness values, which we used in the calculation instead of velocity, were interpolated by shape functions for an arbitrary point within each grid.

Tomographic inversion was performed using a three-step method. First, we determined the initial hypocentre locations and origin times assuming a fixed initial velocity structure. Next, we estimated the one-dimensional velocity profile and recalculated hypocentres and station corrections using a one-dimensional inversion. Lastly, we constructed a tomographic image to obtain three-dimensional velocity perturbations together with recalculated hypocentres and station corrections. This procedure yields more precise hypocentre locations and velocity structure than those based on initial hypocentre locations and the initial one-dimensional velocity structure (e.g. Shibutani *et al.* 2005). We iterated each step three times to obtain the final model.

The initial one-dimensional *P*-wave velocity structure (shown in Fig. 5) was one-dimensional traveltime tomographic model by Hirahara *et al.* (1992). The network used in this study also recorded seismic charges and quarry blasts (denoted by black stars in Fig. 2). Fig. 6 shows the observed, reduced *P*-wave traveltimes from the quarry blasts according to the known epicentral distances, with the theoretical traveltime curve calculated according to the initial one-dimensional velocity structure. The correspondence between the theoretical and observed traveltimes demonstrates the consistency of the initial velocity structure. The initial *S*-wave velocity model was set by dividing *P*-wave one by 1.73.

We used a pseudobending method to perform ray calculation (Um & Thurber 1987), where the initial path is divided into several small segments and changed by a geometric interpretation of the ray equations so that the traveltime along this path is minimized.

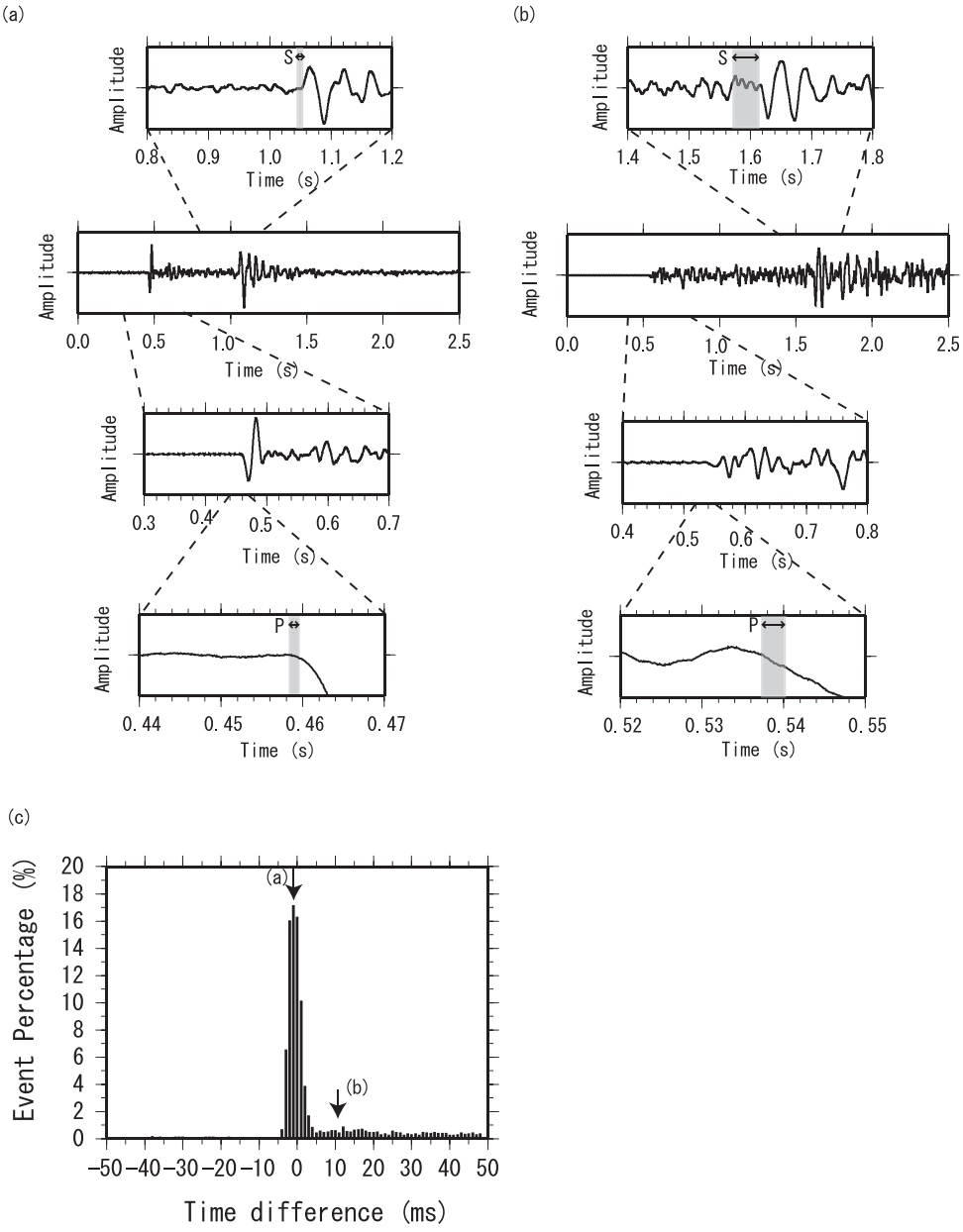

Figure 4. Examples of *P*- and *S*-wave arrival times for waveform records from the station OT01 (a) with a high S/N ratio and (b) with a relatively low S/N ratio. The error for selected *P*-wave arrival times was within a few milliseconds. (c) The distribution of time differences between *P*-wave arrival times estimated visually and by the correlation method for station OT01. Arrows show the *P*-wave arrival time differences for waveforms (a) and (b).

The estimated error in this method is about 1 ms. For fast calculation, we used slowness instead of velocity as unknown parameters as Sekiguchi *et al.* (2004). We assumed the values of the slowness at an arbitrary point as

$$s = \sum_{i=1}^{8} N_i S_i,$$

where N_i is a shape function and S_i is the value of slowness at each gridpoint around the point in question.

The unknown parameters in the matrix are *P*-wave and *S*-wave slownesses, hypocentre locations and origin times. The hypocentre and the slowness matrices were equally weighted for matrix calculation. We added the smoothing matrix at the bottom to stabilize the inversion solution (e.g. Menke 1989). The LSQR method (Paige & Saunders 1982) was used to calculate the inverse matrix due to its sparse nature.

For choosing an appropriate smoothing parameter (the weight of the smoothing matrix), we calculated the root mean square (rms) of traveltime residuals (O-C) for different smoothing parameters. Fig. 7 shows the relationship between the smoothing parameter and the rms for the three-dimensional tomographic image. The error tends to be almost constant when the smoothing parameter is less than 0.5. The error suddenly increases, however, for smoothing parameters larger than 0.5. This smoothing parameter value indicates the lower limit of resolution for the model. Considering errors in estimation of traveltimes, we used this 0.5 smoothing parameter value.

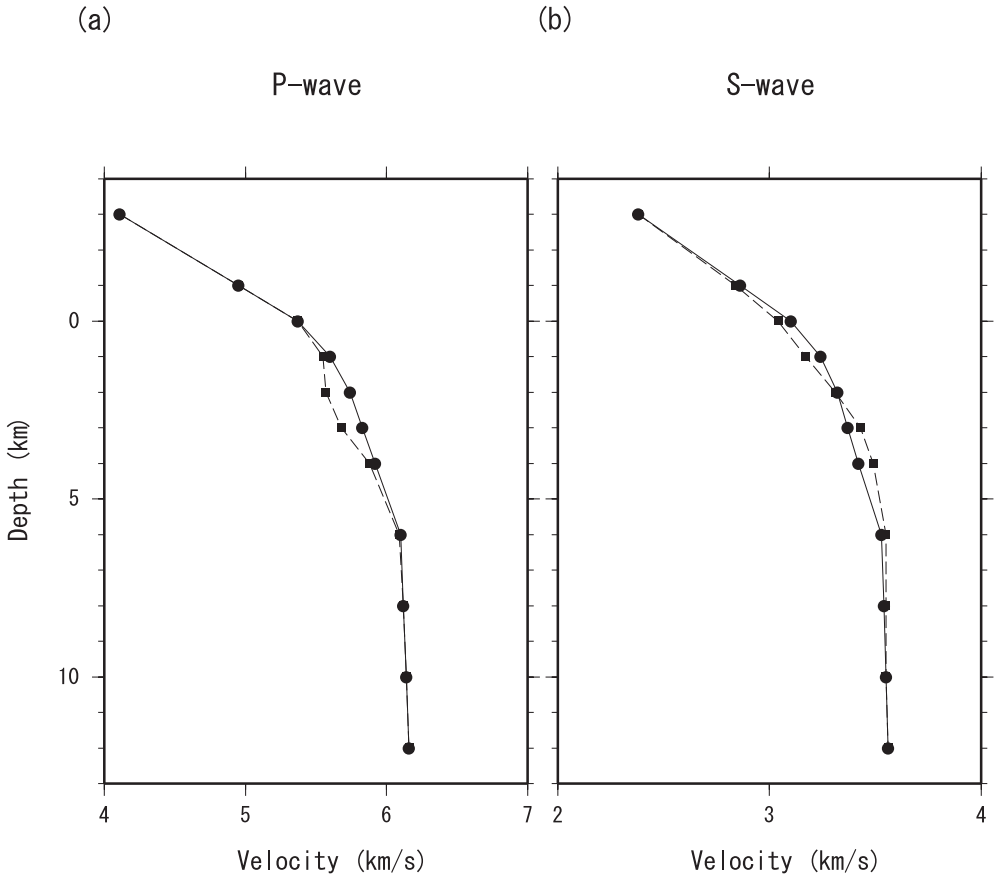

Figure 5. One-dimensional velocity models used as an initial structure in the analysis (solid lines), and obtained from this study (dashed) for (a) *P*- and (b) *S*-wave. Closed circles and squares denote grid locations used for the inversion.

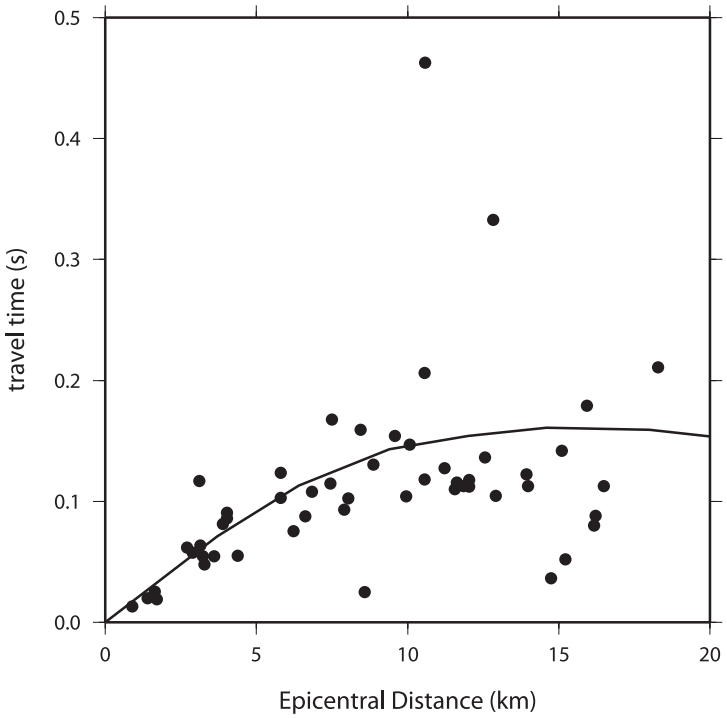

Figure 6. Traveltime diagram for quarry blasts shown in Fig. 2. Traveltimes were reduced with the velocity of 5.5 km s^{-1}. The solid line represents the traveltime curve, which was calculated using the initial velocity structure for the tomographic inversion shown in Fig. 5.

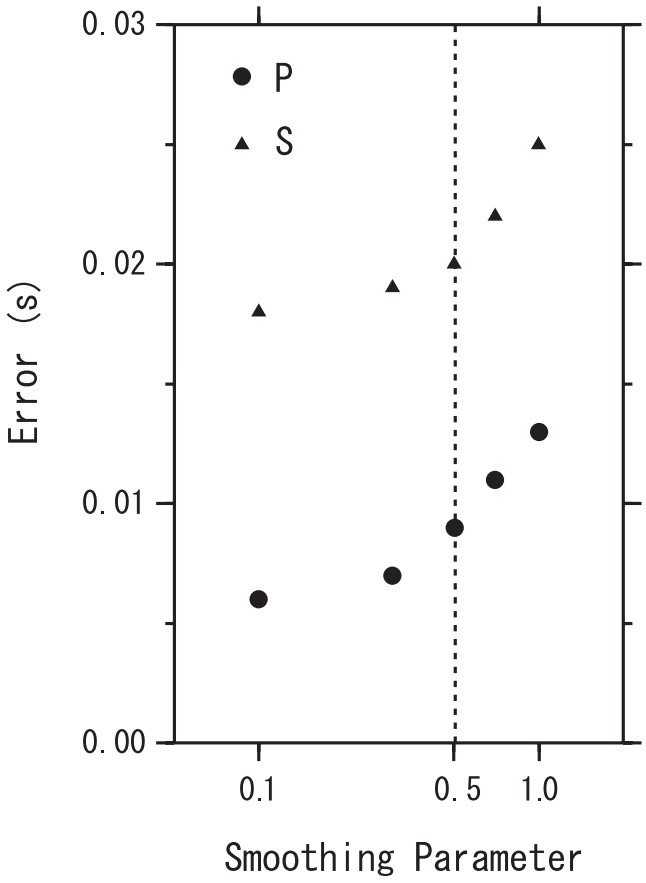

Figure 7. The relationship between smoothing parameter and rms.

5 RESULTS

5.1 Estimated hypocentre locations and velocity structures

Three-dimensional *P*-wave velocity (*Vp*) and *S*-wave velocity (*Vs*) perturbations from the one-dimensional model in the vertical and horizontal planes are shown in Figs 8 and 9 (respectively) along with *Vp*/*Vs* ratios calculated from the magnitudes of *Vp* and *Vs*. We masked the regions which are considered not to have sufficient resolutions (for more details, see Section 5.2). A one-dimensional inversion reduced the rms of O-C for *P*-wave arrivals after the initial hypocentre determination from 18 to 13 ms. Three-dimensional inversion further reduced the errors to 9 ms, which totally reduced the standard deviation by 50 per cent.

5.2 Resolution of the obtained velocity structure

We prepared two kinds of synthetic traveltime data to determine the model resolution. First, we used a checkerboard procedure (Inoue *et al.* 1990) to synthesize traveltimes with 5 per cent velocity perturbations relative to the initial velocity of rays used in the analysis. We estimated the 'restoration ratios' which are defined as ratios of the obtained velocity perturbations to the given ones. For the second data set, we synthesized traveltime data using the final calculated velocity model from this study. Random noise (2 ms for *P*-waves and 30 ms for *S*) was introduced to both synthetic traveltime data sets. We inverted the synthetic data in the same manner as that described in Section 4. We refer to the two velocity models as the 'checkerboard model' and 'synthetic model', respectively.

We show the results of checkerboard model are shown in Figs S1 and S2. Fig. 10 shows the final model from tomographic analysis as well as the synthetic model along the X = 11.5 km cross-section. We drew contour lines in this figure with a restoration ratio of 0.3 from the checkerboard model. The restoration ratio was higher than 0.3 in the central part of the analysis area at depths shallower than 6 km. Comparison of the two models in Fig. 10 shows that the same velocity perturbations were obtained for regions inside the restoration ratio = 0.3 contour lines. This indicates that the velocity perturbations are well resolved given a restoration ratio greater than 0.3.

5.3 Features of hypocentre distribution

Figs 8 and 9 show that most hypocentres are located at depths of 2–6 km along linear features or planes, and do not fall into three-dimensional clusters, even in regions with swarm activity. We identified a 5-km-long, near-vertical hypocentre distribution at depths of 2–6 km near the main shock fault plane, as estimated by Yoshida & Koketsu (1990; that is, $4 < Y < 6$, shown by the F arrows in Figs 8b and 9a). We also identified alignment among hypocentres in the northeastern part of the study region where swarm activity occurs. The most dominant alignments span a distance of 5–10 km, dip 30–60° to the northeast and divide into two parallel planes (shown by arrows S1 and S2 in Figs 9b and c).

5.4 Features of the three-dimensional velocity structure

Hypocentres primarily occur in two regions (regions A and B in Figs 8 and 9). Region A, characterized by low *Vp*, high *Vs* and very low *Vp*/*Vs* ratios (<1.60), was detected in the swarm region at depths of 2 km (Figs 8a, 9a and c). Region B, characterized by high *Vp*, high *Vs* and a slightly low *Vp*/*Vs* (1.65–1.70), is located at depths greater than 3 km and corresponds to swarm hypocentres S1 and S2 (Figs 8b, 9b and c). A neighbouring feature, region C, is characterized by average to high *Vp*, average *Vs* and slightly elevated *Vp*/*Vs* (1.70–1.75), as shown in Figs 8(b), 9(b) and (c). Few earthquakes occur in this region. An additional region with few hypocentres (region C′) exhibited the same velocity trend as region C (Figs 8b and 9b). Regions B and C are distributed parallel to the hypocentre alignments S1 and S2. Hypocentre distributions apparently correlate with *Vp*/*Vs* ratios, but not with *Vp* or *Vs*. We also identified a horizontal, low *Vp* and low *Vs* region with high *Vp*/*Vs* ratios (1.75–1.90) at shallow depths (<2 km). We refer to this region as region L, as shown in Fig. 9. The schematic figure based on X = 11.5 cross-section (i.e. the same as Fig. 9b) is shown in Fig. 11.

6 DISCUSSION

6.1 Velocities for the bedrock matrix in the study region and the nature of velocity changes

The calculated velocity perturbations shown in Figs 8 and 9 are based on the one-dimensional velocity model. In order to interpret the heterogeneous subsurface structure in the study region, it is important to consider velocity changes from velocities of rock matrix, which are velocities of rock without fractures. Takeda *et al.* (1999)

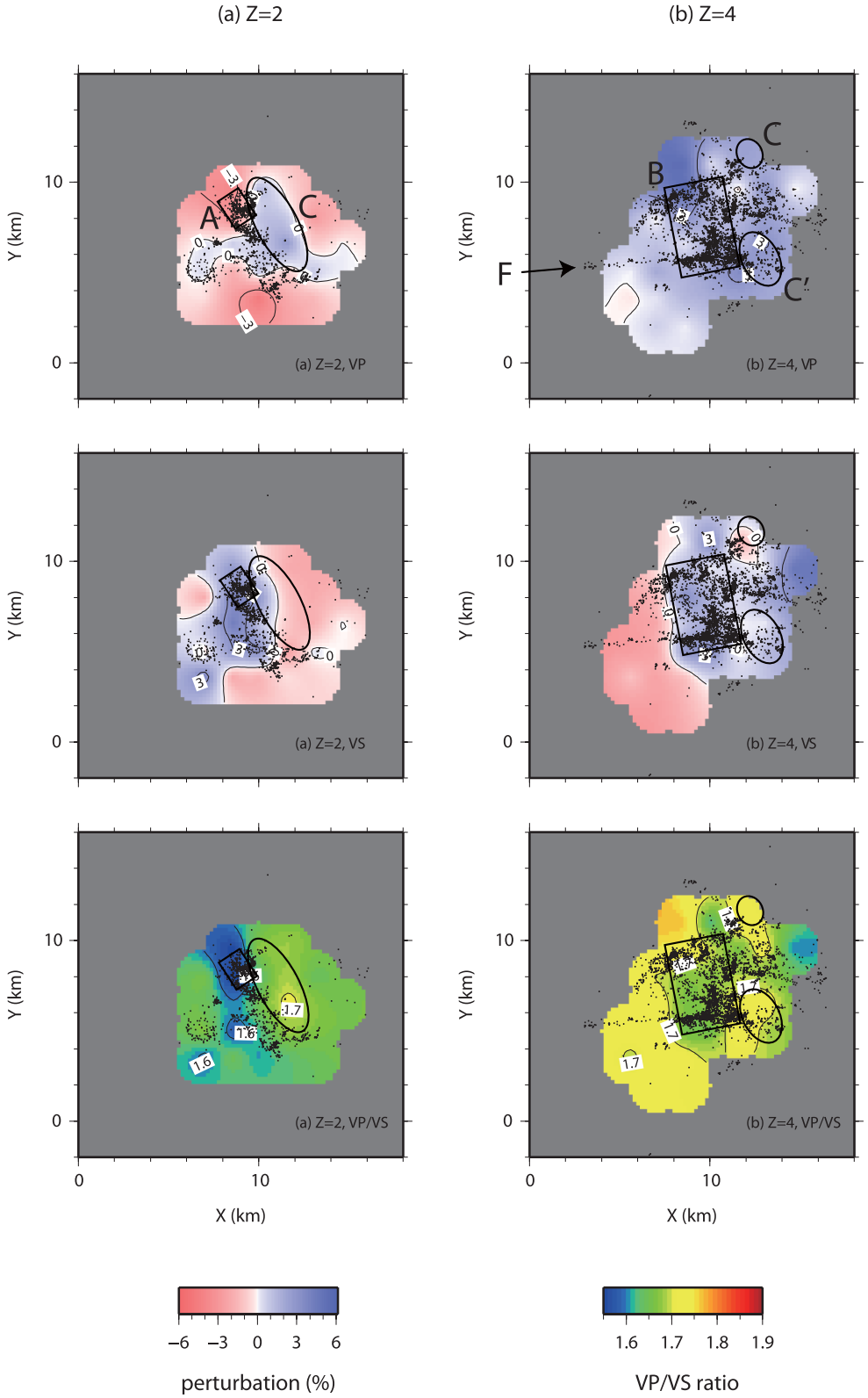

Figure 8. Horizontal view of *P*- and *S*-wave velocity perturbations, and *Vp*/*Vs* ratios obtained from the three-dimensional inversion. Black dots denote the hypocentres. The regions with a restoration rate of less than 0.3 were masked.

determined *Vp* for numerous core samples obtained at depths of 331–722 m from five different boreholes located within the study area. Their *Vp* estimations followed methods of Yamamoto *et al.* (1988, 1991), which estimated *Vp* for a given rock matrix material as the ratio of velocities for saturated versus dry conditions. They found that *Vp* does not vary by more than 3 per cent from average values regardless of rock type, with the exception of slate samples (see Table 1). These results suggest that a *Vp* difference of

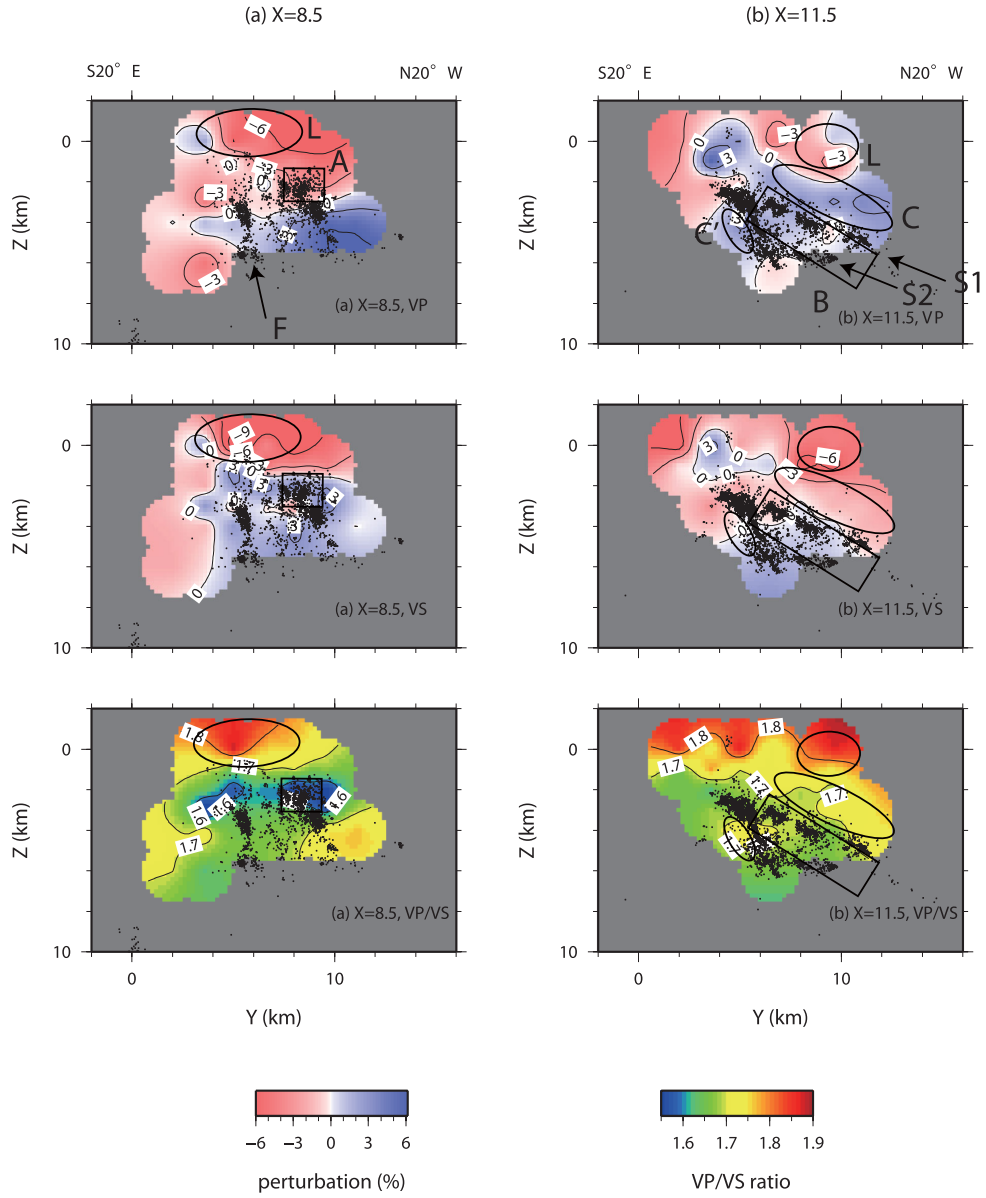

Figure 9. Vertical cross-section of *P*- and *S*-wave velocity perturbations along with *Vp*/*Vs* ratios obtained from the three-dimensional inversion. Black dots denote hypocentres. The regions with a restoration rate of less than 0.3 were masked. The cross-sections for each figure are shown in Fig. 2. The bold line in (a) denotes the fault plane posited by Yoshida & Koketsu (1990). The dashed half ellipse and a blue inverted triangle in (c) show the uplift region (Kimata *et al.* 2004) and the hydrothermal feature with elevated $\delta^{13}C$ values for CO_2 (Takahata *et al.* 2003), respectively.

greater than 3 per cent reflects differences in crack density and/or fluid saturation of rocks. Moreover, *Vp* estimates of Takeda *et al.* (1999) are 3–5 per cent higher than estimates for depths of less than 6 km, as calculated in the one-dimensional model from this study.

Crack densities in the rocks are considered to mainly reflect the magnitudes of *Vs* perturbations, regardless of whether they are saturated or not. *Vp*/*Vs* ratios are affected by aspect ratios and saturation of cracks. If the aspect ratios are the same, higher *Vp*/*Vs* ratios indicate high saturation (Takei 2002). Therefore, the regions with low *Vs* and high *Vp*/*Vs* ratios have lots of saturated cracks (probably with moderate aspect ratios). On the other hand, low *Vp*/*Vs* ratios indicate that the cracks are not saturated.

6.2 Mantle-derived fluids near the surface

Fluids originating from the mantle were detected from a hydrothermal feature above the low-velocity region L, indicated by the blue inverted triangle in Fig. 9(c) (Takahata *et al.* 2003). The relatively low *P*- and *S*-wave velocity estimates along with the high *Vp*/*Vs* ratios in region L suggest a dense volume of cracks saturated with mantle-derived fluids, as described in Section 6.1. This inference is supported by JMA catalog entries showing deep, low-frequency events recorded at depths of 15–50 km just beneath the study area, which are interpreted as evidence of fluid movement (Ohmi & Obara 2002). Surface uplift was also observed in the area marked by the black, dashed half ellipse in Fig. 9(c) (Kimata *et al.* 2004). These observations along with other researches suggest that fluids

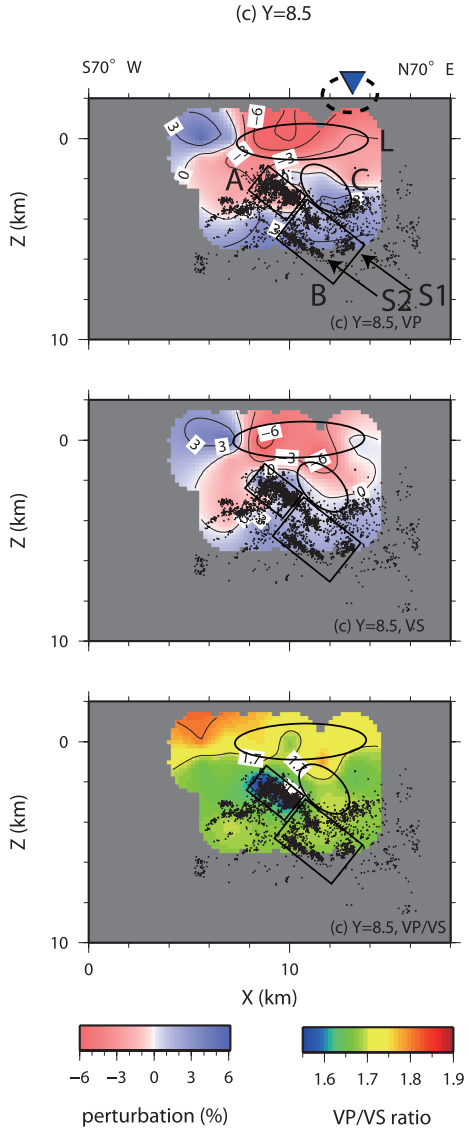

Figure 9. *(Continued.)*

originate in the mantle and ascend through the study area to accumulate near the surface.

6.3 The main shock fault plane

We detected a near-vertical hypocentre alignment feature (referred to as 'F') near the hypocentre of the 1984 western Nagano Prefecture earthquake. We think that this alignment corresponds to the main shock fault plane because it shows similar attitudes to those of the fault plane estimated in Yoshida & Koketsu (1990) and the events had strike-slip focal mechanisms (Yukutake *et al.* 2010). The fault plane estimated in this study was located at a distance of 1–2 km from that estimated by Yoshida & Koketsu (1990), as shown in Fig. 9(a). This offset is possibly due to the limited coverage of the permanent JMA network (stations spaced about 50 km apart), as this was the only network previously available in the study area. We identified the main shock fault from hypocentral distributions precisely determined by a seismic network with a much higher station density.

Surface rupture is an important factor in predicting strong motion and earthquake hazards. No apparent surface rupture occurred during the 1984 western Nagano Prefecture earthquake (Umeda *et al.* 1987), in spite of its shallow focal depth and magnitude. The low-velocity region L is located at the upper edge of the hypocentre alignment F (Fig. 9a) and the large slip regions of the main shock (Yoshida & Koketsu 1990). These low *Vp* and *Vs* regions were attributed to saturated cracks described in Section 6.2. Numerical simulations have shown that fluid-saturated material in the drainage state decreases the pore pressure along the extensional side to arrest rupture propagation (Viesca *et al.* 2008; Samuelson *et al.* 2011). This low-velocity region could have prevented the rupture from extending upwards to the surface (as denoted by a dashed line in the schematic figure, Fig. 11).

Regions C′ is located at the eastern edge of the main shock fault (Fig. 8b), according to the hypocentre distribution of alignment F. The distributions of *Vp*/*Vs* ratios, instead of low velocities as inferred in Hirahara *et al.* (1992), may be considered to stop the rupture propagation.

6.4 Relationship between swarm activity and the velocity structure

In the swarm activity region, most hypocentres are distributed within two regions, regions A and B, which exhibit low to very low *Vp*/*Vs* ratios. We investigated the relationship between the hypocentral locations and the velocity structure of these regions. Fig. 12 shows histograms of earthquake frequencies, grid frequencies and earthquake frequencies per grid, according to *Vp*/*Vs* ratios, for regions with a restoration ratio greater than 0.3. Hypocentre histograms show two local peaks corresponding to *Vp*/*Vs* ratios of 1.58–1.60 and 1.68–1.70, while grid numbers according to the *Vp*/*Vs* ratios are normally distributed with an average value of around 1.73. This indicates that hypocentres are not independent of *Vp*/*Vs* ratios. Hypocentre frequency according to *Vp*/*Vs* ratios concentrate at *Vp*/*Vs* ratios of 1.56–1.60 and 1.68–1.70, which correspond to regions A and B, respectively. Regions C and C′ (with 1.70–1.75 *Vp*/*Vs* ratios) have relatively few earthquakes compared to other areas of the grids.

Assuming a matrix *P*-wave velocity of 6.24 km s^{-1} (Takeda *et al.* 1999), the *Vp* for regions A and B is about 10 and 5 per cent lower than the *P*-wave velocity for the matrix. Assuming a *Vp*/*Vs* ratio of 1.73 for the bedrock matrix, the *Vs* for regions A and B is several percent lower than the *S*-wave velocity for the matrix. On the other hand, in regions C and C′, where few swarm activities are observed, *Vp*/*Vs* is normal (around 1.73) and *Vs* is lower than that in regions A and B and about 7 per cent lower than the bed rock one. According to the description in Section 6.1, these results indicate that crack densities are high and they are saturated in regions C and C′, while there exist open (or a little saturated) cracks in regions A and B. The portions of saturated cracks may be responsible for the difference in *Vp*/*Vs* ratios. These observations are consistent with the results of a three-dimensional electrical resistivity survey that showed low resistivity in regions C and C′, compared with the surrounding regions (Yoshimura *et al.* 2011).

Lin & Shearer (2009) and Kato *et al.* (2010) similarly found that regions in swarm source regions have low *Vp*/*Vs* ratios. These workers interpreted the anomalies as evidence of cracks with up to several percent saturation. The fact that the hypocentral distributions show a linear or a planar trend suggests that the swarm events occur on the pre-existing fracture systems. Pore pressure likely increases when the fluids, which are considered to be supplied from the mantle, migrate into these open (or a little saturated) cracks, as denoted by red arrows in Fig. 11. This leads to earthquake

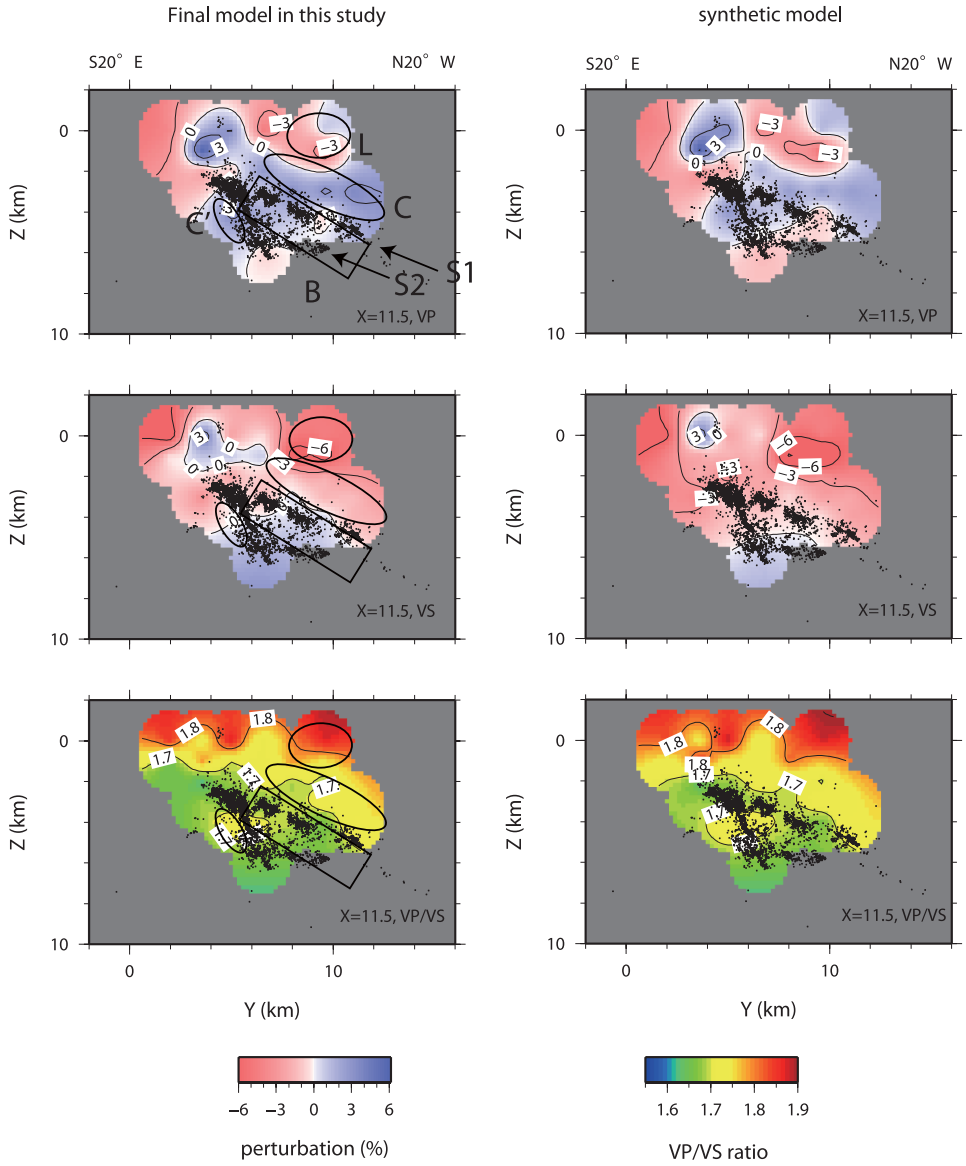

Figure 10. Comparison of the tomographic results from the cross-section shown in Fig. 2 (b). The left panel shows the final tomographic model determined by this study (same as Fig. 9b). The right panel shows the synthetic model. We show the regions with a restoration ratio greater than 0.3, as calculated from the checkerboard model.

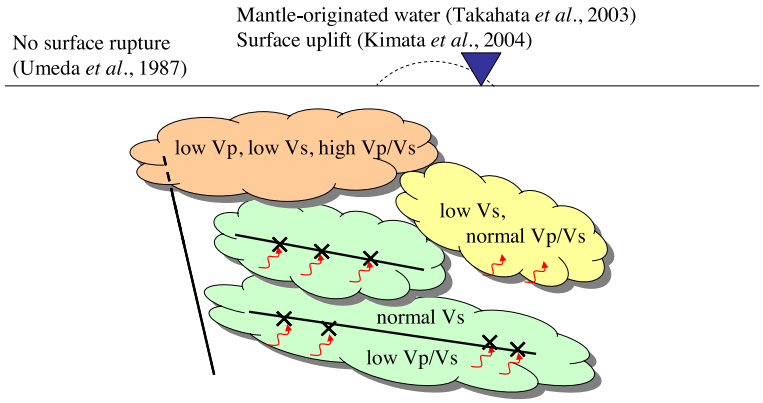

Figure 11. The schematic figure of the results in this study. Crosses and red arrows denote the earthquake occurrence and fluid flows, respectively. Solid lines denote the hypocentre distributions, while a dashed line represents that the main shock rupture did not reach the ground surface. The dashed half ellipse and a blue inverted triangle show the uplift region (Kimata *et al.* 2004) and the hydrothermal feature with elevated $\delta^{13}C$ values for CO_2 (Takahata *et al.* 2003), respectively.

Table 1. *P*-wave velocities for several bedrock types after Takeda *et al.* (1999).

Location	Depth (m)	Rock type	*P* wave velocity (km s^{-1})
OT-2	331	Dacite	6.24
OT-2	448	Porphyrite	6.26
OT-2	722	Rhyolite	6.22
OT-3	376	Sandstone	6.45
OT-3	600	Sandstone	6.27
OT-4	705	Slate	5.59
OT-5	470	Sandstone	6.17

occurrence (crosses in Fig. 11) in regions A and B. However, if the cracks are saturated as in regions C and C′, pore pressure may not change so much along with fluid intrusion, resulting in small number of earthquakes.

Many tomographic studies have addressed source regions for large inland earthquakes (e.g. Zhao & Negishi 1998; Tian *et al.* 2007; Okada *et al.* 2008) and swarms (e.g. Vidale & Shearer 2006; Kato *et al.* 2010; Yukutake *et al.* 2011). These studies have suggested the existence of underlying subsurface fluids and swarm migration due to their diffusion. Fluid behaviour in the subsurface remains poorly understood, however, due to limited information regarding subsurface structure. Precise modelling reported by this study includes velocity properties of the medium imaged at a resolution of 1.5 km and provides a detailed description of fluid behaviour and its relationship to swarm seismicity. This provides information for other study areas where earthquake swarms occur adjacent to volcanoes.

7 CONCLUSIONS

We conducted a three-dimensional traveltime tomography in and around the source region of the 1984 western Nagano Prefecture earthquake (M_j 6.8). We used around 220 000 highly accurate *P*-wave arrival times (with 2 ms errors) and 180 000 *S*-wave arrival times (with 20 ms errors) from a dense seismic network (station spacing 1–4 km) to determine highly accurate hypocentre distributions and detailed three-dimensional velocity structure at depths of 2–6 km. Most hypocentres aligned along linear features or planes, rather than in three-dimensional clusters, even in the swarm activity region. One of the hypocentre alignments coincides with the main shock fault. Regions with high and normal *Vp*/*Vs* ratios, assumed to have a high and a relatively high density of fluid-saturated cracks, were detected at the upper limit and eastern edge of this hypocentre alignment, respectively. The main shock rupture propagation was apparently affected by characteristics of the surrounding medium. Hypocentral distributions in the swarm regions correspond to regions with low *Vp*/*Vs* ratios. The difference between the velocity in these regions and measured matrix velocities indicates the presence of unsaturated cracks. Swarm activity occurs when fluids, inferred from the distribution of low-velocity regions and from past studies of the swarm region, migrate into these cracks.

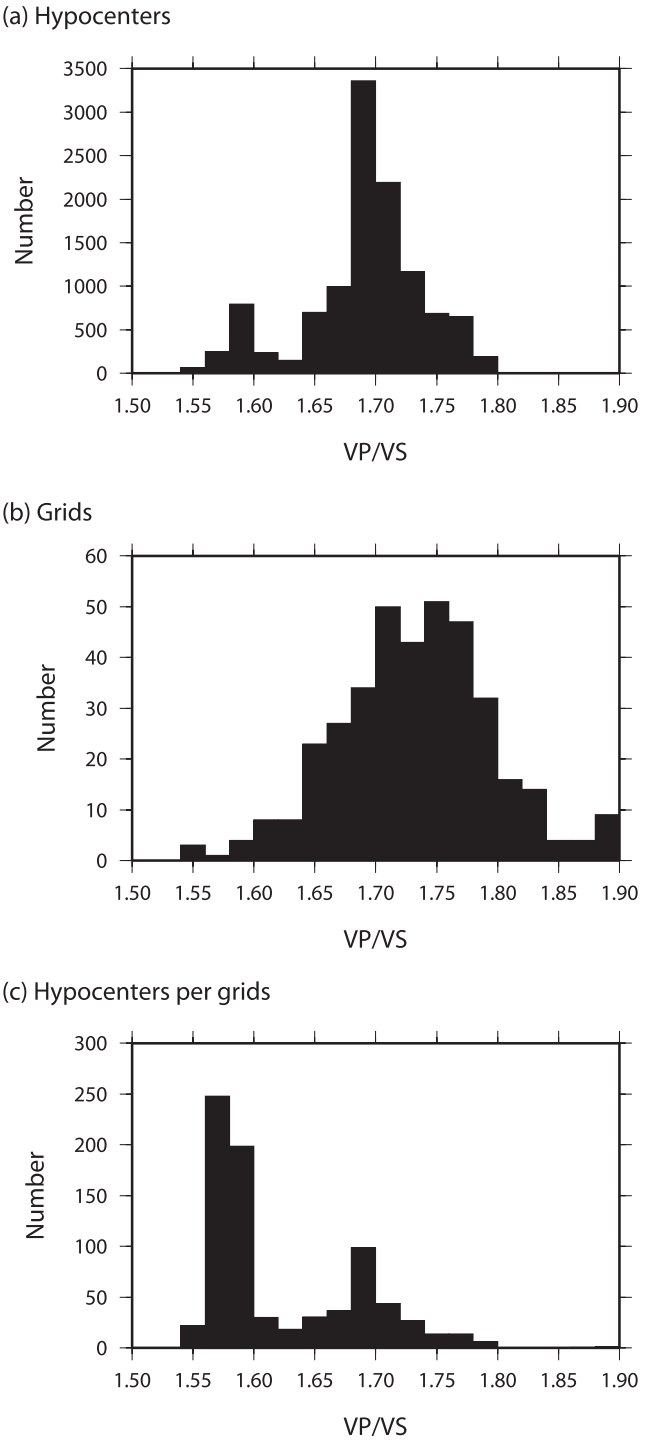

Figure 12. Histograms of estimated hypocentre frequencies, the numbers of the grids and the numbers of the hypocentres per grid, according to *Vp*/*Vs* ratios for regions with a restoration ratio larger than 0.3, as calculated by the checkerboard model.

ACKNOWLEDGEMENTS

We thank Shiro Ohmi for developing the novel data processing system used during the first several years of this research effort. We also thank Eiji Yamamoto, Hisao Ito, Yasuto Kuwahara and Takao Ohminato for their very helpful contributions regarding borehole observations. We are grateful to Kaori Takai for her help with data processing. Comments from two anonymous reviewers helped us to improve the manuscript. We used the General Mapping Tool (Wessel & Smith 1991) for drafting the figures presented in this manuscript. This work was partially supported by JSPS.KAKENHI (19204043), Japan.

REFERENCES

Cheng, X., Niu, F., Silver, P.G., Horiuchi, S., Takai, K., Iio, Y. & Ito, H., 2007. Similar microearthquakes observed in western Nagano, Japan, and implications for rupture mechanics, *J. geophys. Res.,* **112,** B04306, doi:10.1029/2006JB004416.

Hasegawa, A., Nakajima, J., Uchida, N., Okada, T., Zhao, D., Matsuzawa, T. & Umino, N., 2009. Plate subduction, and generation of earthquakes and magmas in Japan as inferred from seismic observations: an overview, *Gondwana Res.,* **16,** 370–400.

Hirahara, K. The Members of the 1986 Joint Seismological Research In Western Nagano Prefecture, 1992. Three-dimensional P and S wave velocity structure in the focal region of the 1984 Western Nagano Prefecture Earthquake, *J. Phys. Earth,* **40,** 343–360.

Iio, Y. *et al.*, 1999. Slow initial phase generated by microearthquakes occurring in the Western Nagano Prefecture, Japan. - the source effect, *Geophys. Res. Lett.,* **26,** 1969–1972.

Iio, Y., Sagiya, T., Kobayashi, Y. & Shiozaki, I., 2002. Water-weakened lower crust and its role in the concentrated deformation in the Japanese Islands, *Earth planet. Sci. Lett.,* **203,** 245–253.

Inoue, H., Fukao, Y., Tanabe, K. & Ogata, K., 1990. Whole mantle P-wave travel time tomography, *Phys. Earth planet. Inter.,* **59,** 294–328.

Kasaya, T. & Oshiman, N., 2004. Lateral inhomogeneity deduced from 3-D magnetotelluric modeling around the hypocentral area of the 1984 Nagano Prefecture earthquake, central Japan, *Earth Planets Space,* **56,** 547–552.

Kato, A., Sakai, S., Iidaka, T., Iwasaki, T. & Hirata, N., 2010. Non-volcanic seismic swarms triggered by circulating fluids and pressure fluctuations above a solidified diorite intrusion, *Geophys. Res. Lett.,* **37,** L15302, doi:10.1029/2010GL043887.

Kimata, F. *et al.*, 2004. Ground uplift detected by precise leveling in the Ontake earthquakes swarm area, central Japan in 2002–2004, *Earth Planets Space,* **56,** e45–e48.

Li, Y.-G., Aki, K., Adams, D., Hasemi, A. & Kee, W.H.K., 1994. Seismic guided waves trapped in the fault zone of the Landers, California, earthquake of 1992, *J. geophys. Res.,* **99,** 11 705–11 722.

Lin, G. & Shearer, P.M., 2009. Evidence for waterfilled cracks in earthquake source regions, *Geophys. Res. Lett.,* **36,** L17315, doi:10.1029/2009GL039098.

Menke, W., 1989. *Geophysical Data Analysis: Discrete Inverse Theory,* 289 p, Academic Press.

Mizuno, T., Nishigami, K., Ito, H. & Kuwahara, Y., 2004. Deep structure of the Mozumi-Sukenobu fault, central Japan, estimated from the subsurface array observation of fault zone trapped waves, *Geophys. J. Int.,* **159,** 622–642.

Ohmi, S. & Obara, K., 2002. Deep low-frequency earthquakes beneath the focal region of the Mw 6.7 2000 Western Tottori earthquake, *Geophys. Res. Lett.,* **29,** 1807, doi:10.1029/2001GL014469.

Okada, T., Yaginuma, T., Umino, N., Matsuzawa, T., Hasegawa, A., Zhang, H. & Thurber, C.H., 2006. Detailed imaging of the fault planes of the 2004 Niigata-Chuetsu, central Japan, earthquake sequence by double-difference tomography, *Earth planet. Sci. Lett.,* **244,** 32–43.

Okada, T., Umino, N. & Hasegawa, A., 2008. Imaging inhomogeneous seismic velocity structure in and around the fault plane of the 2008 Iwate-Miyagi, Japan, Nairiku Earthquake (M7.2) – spatial variation in depth of seismic-aseismic transition and possible high-T/overpressurized fluid distribution, *American Geophysical Union, Fall Meeting 2008*, T51D-02.

Ooida, T., Yamazaki, F., Fujii, I. & Aoki, H., 1989. Aftershock activity of the 1984 Western Nagano Prefecture Earthquake, central Japan, and its relation to earthquakes swarms, *J. Phys. Earth,* **37,** 401–416.

Paige, C.C. & Saunders, M.A. 1982. LSQR: an algorithm for sparse linear equations and sparse least squares, *ACM Trans. Math. Softw.,* **8,** 43–71.

Research Group for Active Faults of Japan, 1991. *Active Faults in Japan: Sheet Maps and Inventories (Revised Edition) (in Japanese with English Summary),* University of Tokyo Press.

Samuelson, J., Elsworth, D. & Marone, C., 2011. Influence of dilatancy on the frictional constitutive behavior of a saturated fault zone under a variety of drainage conditions, *J. geophys. Res.,* **116,** B10406, doi:10.1029/2011JB008556.

Sekiguchi, S., Iio, Y., Ohmi, S., Ito, H. & Horiuchi, S., 2004. Three-dimensional velocity structure and the possibility of its time variation at the Western Nagano Prefecture region using dense seismic network (in Japanese with English abstract), *J. seism. Soc. Jpn.,* **57,** 55–61.

Shearer, P., Hauksson, E. & Lin, G., 2005. Southern California hypocenter relocation with waveform cross-correlation. Part 2: results using source-specific station terms and cluster analysis, *Bull. Soc. seism. Am.,* **95,** 904–915.

Shibutani, T. & Katao, H. Group for the Dense Aftershock Observations of the 2000 Western Tottori Earthquake, 2005. Very dense aftershock observations of the 2000 Western Tottori Earthquake (Mj = 7.3) in southwestern Honshu, Japan: high resolution aftershock distribution, focal mechanisms and 3-D velocity structure in the source region, *Earth Planets Space,* **57,** 825–838.

Takahata, N., Yokochi, R., Nishio, Y. & Sano, Y., 2003. Volatile element isotope systematics at Ontake volcano, *Jpn. Geochem. J.,* **37,** 299–310.

Takeda, J., Iio, Y., Kobayashi, Y., Yamamoto, K., Sato, H. & Ohmi, S., 1999. The relationship between seismicity and fluid existing in the crust inferred from V_p/V_s ratio -An Analysis of the data from the dense microseismic networks installed in the Western Nagano Prefecture Region-, (in Japanese with English abstract), *J. seism. Soc. Jpn.,* **2**(51), 419–430.

Takei, Y., 2002. Effect of pore geometry on V_p/V_s: from equilibrium geometry to crack, *J. geophys. Res.,* **107,** doi:10.1029/2001JB000522.

Tanaka, A. & Ito, H., 2002. Temperature at base of the seismogenic zone and its relationship to the focal depth of Western Nagano Prefecture area (in Japanese with English abstract), *J. seism. Soc. Jpn.,* **55,** 1–10.

Tian, Y., Zhao, D. & Teng, J., 2007. Deep structure of Southern California, *Phys. Earth planet. Inter.,* **165,** 93–113.

Um, J. & Thurber, C., 1987. A fast algorithm for two-point seismic ray tracing, *Bull. seism. Soc. Am.,* **77,** 972–986.

Umeda, Y., Kuroiso, A., Ito, K. & Muramatu, I., 1987. Highaccelerations produced by the Western Nagano Prefecture, Japan, earthquake of 1984, *Tectonophysics,* **141,** 335–343.

Venkataraman, A., Beroza, G.C., Ide, S., Imanishi, K., Ito, H. & Iio, Y., 2006. Measurements of spectral similarity for microearthquakes in western Nagano, Japan, *J. geophys. Res.,* **111,** B03303, doi:10.1029/2005JB003834.

Vidale, J.E. & Shearer, P.M., 2006. A survey of 71 earthquake bursts across southern California: exploring the role of pore fluid pressure fluctuations and aseismic slip as drivers, *J. geophys. Res.,* **111,** B05312, doi:10.1029/2005JB004034.

Viesca, R.C., Templeton, E.L. & Rice, J.R., 2008. Off-fault plasticity and earthquake rupture dynamics: 2. Effects of fluid saturation, *J. geophys. Res.,* **113,** B09307, doi:10.1029/2007JB005530.

Wessel, P. & Smith, W.H.F., 1991. Free software helps map and display data, *EOS Trans.,* **72,** 441.

Yamamoto, K., Kato, N. & Hirasawa, T., 1988. Estimation of matrix P-wave velocity of a rock sample – by measurement of elastic velocity in the saturated and dry conditions – (in Japanese), *Proc. J. seism. Soc. Jpn.,* **2,** 77.

Yamamoto, K., Kato, N. & Hirasawa, T., 1991. Estimation of matrix P-wave velocity of a rock sample (Part 2) (in Japanese), *Proc. J. seism. Soc. Jpn.,* **1,** 129.

Yoshida, S. & Koketsu, K., 1990. Simultaneous inversion of waveform and geodetic data for the rupture process of the 1984 Naganoken-Seibu, Japan, earthquake, *Geophys. J. Int.,* **103,** 355–362.

Yoshimura, R., Oshiman, N., Kasaya, T., Iio, Y. & Omura, K., 2011. On the heterogeneous electrical structure around earthquake swarm region, *The XXV IUGG General Assembly Abstracts*, JA01–5268.

Yukutake, Y., Iio, Y. & Horiuchi, S., 2010. Detailed spatial changes in the stress field of the 1984 western Nagano earthquake region, *J. geophys. Res.,* **115,** B06305, doi:10.1029/2008JB006111.

Yukutake, Y., Ito, H., Honda, R., Harada, M., Tanada, T. & Yoshida, A., 2011. Fluid-induced swarm earthquake sequence revealed by

precisely determined hypocenters and focal mechanisms in the 2009 activity at Hakone volcano, Japan, *J. geophys. Res.,* **116,** B04308, doi:10.1029/2010JB008036.

Zhao, D. & Negishi, H., 1998. The 1995 Kobe earthquake: seismic image of the source zone and its implications for the rupture nucleation, *J. geophys. Res.,* **103,** 9967–9986.

SUPPORTING INFORMATION

Additional Supporting Information may be found in the online version of this article:

Figure S1. Horizontal view of *P*- and *S*-wave velocity perturbations in the checkerboard test. Black dots denote the hypocentres.

Figure S2. Vertical cross-sections of *P*- and *S*-wave velocity perturbations in the checkerboard test. Black dots denote the hypocentres (http://gji.oxfordjournals.org/lookup/suppl/doi:10.1093/gji/ggt312/-/DC1).

Please note: Oxford University Press are not responsible for the content or functionality of any supporting materials supplied by the authors. Any queries (other than missing material) should be directed to the corresponding author for the article.